Thrust Force for Drone Propeller with Normal and Serrated Trailing Edge

Mohd Zaki Bahrom[1], Bukhari Manshoor[1,*], Badrul Aisham Md Zain[1], Izzuddin Zaman[1], Djamal Hissein Didane[1], Reazul Haq Abdul Haq[1], Mohd Nizam Ibrahim[2]

[1] Faculty of Mechanical and Manufacturing Engineering, Universiti Tun Hussein Onn Malaysia, Batu Pahat 86400, Malaysia
[2] Maxpirations (M) Sdn Bhd, 1st Floor, Sura Gate Commercial Centre, Jalan Sura Jeti, 23000 Dungun, Terengganu, Malaysia

ARTICLE INFO

ABSTRACT

The drone becomes more recognized in the civilian sector; the drone's popularity becomes increases as time goes by. Nevertheless, despite the excitement of flying drones, several types of issues occur caused by the drone. In some circumstances, the aeroacoustics noise is a big concern, and quiet drone propellers would be more environmentally friendly to the surrounding area. Moreover, the noise from the drone can be a nuisance for the surrounding population and animals. Therefore, a solution needs to be proposed to reduce the sound level produced by the drone so that drone can be piloted in a surrounding area without breaking any noise level limit set by the government. Hence, the propeller's serrated trailing edge type is the proposed solution to this problem. The serrated trailing edge propeller can reduce several drone noise decibels based on past research. Thus, an investigation is conducted to study the thrust force between the normal propeller and the serrated propeller. The aerodynamic performance of the serrated propeller is analysed using computational fluid dynamic simulation and compared to that of the normal propeller. Ansys Fluent 2021 is used to solve the dependable RNG k-epsilon turbulence model. The thrust force, thrust coefficient, and lift coefficient operating on both propellers were all simulated. The results obtained by the transient approach for propellers have been validated by earlier experimental studies.

1. Introduction

Drone, which were initially designed for military use, have seen rapid growth and advances, and have found their way into consumer electronics. Initially, they were used as weapons in the form of remotely guided aerial missile launchers. However, drone's popularity has increased in civilian use and has a wide range of applications today, especially in the form of small quadcopters and octocopters [1]. Drones are also used for various purposes, including climate monitoring, shipping supplies, assisting in search and rescue operations, and filming and photography. Many drones can now be deployed and controlled with minimal experience, thanks to advancements in control technology. Drone becoming more available to a broader range of operators, thanks to the relatively

---

Corresponding author.
E-mail address: bukhari@uthm.edu.my

low cost of most models. Besides, unmanned aerial vehicles (UAV) have a wider range of motion than manned aircraft [2-5]. They can travel lower and, in more directions, making it easier for them to navigate usually difficult-to-reach areas. Nevertheless, despite the excitement of getting to fly the drones, several types of issues arise caused by the drone. In some circumstances, the aeroacoustics noise is a big concern, and quiet drone propellers would be more environmentally friendly to the surrounding area. Generally, the noise produces from the drone are comes from different parts of the drone, which are motors, propeller, and aircraft body designs [6-9].

For comparison, a commercial drone which is DJI M200, have a noise profile of 47.5 dBA, which is in a slow fight with level flyover normalized to a 400-foot height above the microphones to the highest of 74.5 dBA that arrives from North at 100-foot cruise vertical descent to the landing pad [10]. If the mechanical noise is sufficiently addressed in modern rotating machinery, the aerodynamic noise generated by the blades is often considered to be the major noise source. Aerodynamic noises can be divided into two categories. The first is turbulent inflow noise, which is created by upstream atmospheric turbulence interacting with the blade and is dependent on atmospheric conditions. The airfoil self-noise, which is created by the blade in an undisturbed inflow, is the second type. Self-noise in airfoils is further separated into two noise mechanisms: trailing edge and blade tip vortex noises [11,12].

Drone made by the most manufacturers usually produce acoustic footprint that closes to the excessive noise level which is 85dBA. By using the serrated trailing edge propeller, the noise level produces by the drone will reduce to a much bearable level [13-15]. Despite that, for the drone's performance, the thrust force of the propeller cannot be compromised. Hence, it is crucial to analyse the performance of the normal and serrated trailing edge so that the design of the drone propeller can give the best performance for both in terms of noise emission and the thrust performance of the drone's propeller. This study wants to determine the drone force's thrust of the normal and serrated trailing edge and make a comparison of the thrust force for both types of drone propellers. The significance of this study is to determine whether, by using the serrated trailing edge propeller, the drone will lose its performance, remain constant or reduce slightly. The result will help a researcher understand the propeller's lift and drag properties by analysing the normal propeller and the trailing edge performance. Besides that, civilians can change their propeller design instead of the normal propeller into a serrated trailing edge propeller to reduce the noise emitted from their drones.

2. Methodology

The methodology for this study was divided into three stages. The first stage was the geometry design and development, followed by simulation work. The results from the simulation work will be verified.

2.1 Propeller Model

There are several elements that can analyses in the propeller. According to Rajan Gill and Muhammad [16,17], the practice of splitting a propeller blade into tiny pieces or "elements" is known as blade element theory. Each blade element's quasi-steady aerodynamic forces will be calculated. For the sake of brevity, a function's dependent on Ω, V and β, and will be removed. The aerodynamic lift and drag forces of the blade element are defined as when the fluid is in steady state motion.

$$dL(y,\psi) = \frac{1}{2}\rho U(y,\psi)^2 C_L\big(\alpha(y,\psi)\big)c(y)dy \qquad (1)$$

$$d\widetilde{D}(y,\psi) = \frac{1}{2}\rho U(y,\psi)^2 C_D\big(\alpha(y,\psi)\big)c(y)dy \qquad (2)$$

where U = $\sqrt{U_T^2 + U_P^2}$ is the air density, and dL and dD˜ are the aerodynamic forces acting perpendicular and tangential to the blade element's freestream velocity at distance y from the rotor's center. The angle φ denotes the azimuth angle of a propeller blade within the rotor disc, with $\varphi = 0$ being the point where the propeller is parallel to the projection of $\underset{V}{\rightarrow}$ on the rotor disc plane.

2.2 Normal Propeller

The propellers used in UAVs are typically smaller than 24 inches in diameter. As a result, in the current study, the advanced precision composites (APC) Slow Flyer propeller is chosen as the standard design since it is one of the most used blades for UAVs and because experimental data is readily available [18 - 20]. The commercially available CFD solution FLUENT was used to simulate this propeller numerically. CFD simulations were run for a variety of propeller advance ratios, as shown in Table 1.

Table 1
Simulation flow conditions

Advanced coefficient, J	Free stream velocity, m/s
0.192	2.4384
0.236	2.9972
0.282	3.5814
0.334	4.2418
0.383	4.8641
0.432	5.4864
0.486	6.1722
0.527	6.6929
0.573	7.2771
0.628	7.9576
0.659	8.3693
0.717	9.1059
0.773	9.8171
0.799	10.1473

The APC Slow Flyer is a two-bladed propeller with a fixed pitch and a diameter of 0.254 m. It has a set pitch and a diameter of 0.254 m. The propeller is made from thin airfoil profiles with a unique mix of low Reynolds number and high thrust. Figure 1 shows an Eppler E63 with a Clark-Y airfoil near the tip inserted to make a sharp leading edge blade design. The pitch of 0.1778 m results in a pitch-to-diameter ratio of 0.7, which is typical of off-the-shelf propellers [21].
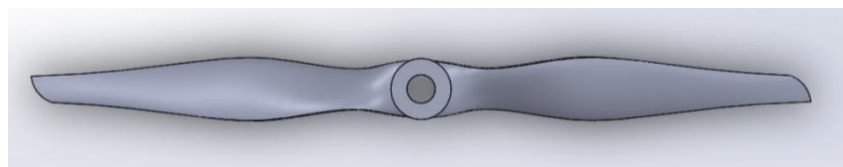

Fig. 1. Model of the propeller by Solidworks

Table 2
Propeller properties

Properties	Value
Density	2.4384
Young's modulus	2.9972
Poisson's ratio	3.5814
Stress at break	4.2418
Strain at break	4.8641

2.3 Sawtooth Serrated Trailing Edge

In the 2D flat plate and airfoil research, sawtooth serration was always applied to the propeller's trailing edge as a feature. Meanwhile, in Oerlemanse's rotating motion investigation, the author applied the serration straight to the trailing edge of the wind turbine at the tip area. As a result, one form of sawtooth serration was applied to the baseline propeller's trailing edge in this investigation, as shown in Figure 2. The uniform serrations have a width-to-height ratio of 0.6, with a height of 4mm and a width of 2.4mm.

To reduce trailing edge noise, the height of the serration should be greater than a fifth of the boundary layer thickness at the trailing edge, and the inclined angle cannot be greater than 45 degrees. These criteria will be met by the study's choice of a 4mm height. Furthermore, the width-to-height ratio employed in this study is less than 4. Due to the restricted in computer specification, the length of the serration will be half the length of the propeller blade.
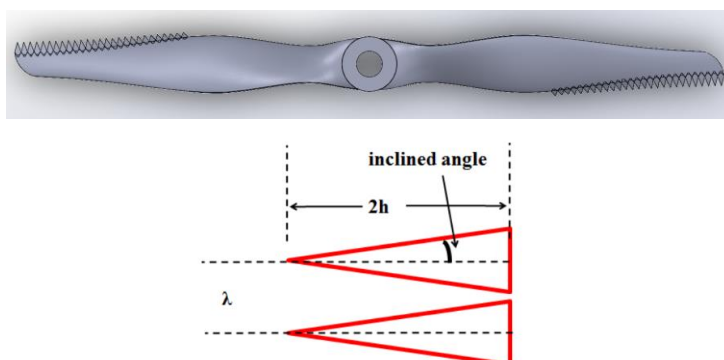
Fig. 2. Sawtooth trailing edge model in Solidworks and geometries of sawtooth serrated trailing edge [4]

The numerical predictions in this work were made with the commercial CFD solver ANSYS FLUENT. The flow around the propeller was quantitatively predicted using the Multiple Reference Frame model (MRF). Figure 3(a) shows the domain definition and illustration. The domain is divided into two parts: a global stationary domain and a rotating domain with subdivided rotating regions. As shown in Figure 3(b), the rotational domain is defined by a smaller cylinder that completely encloses the blade and hub.
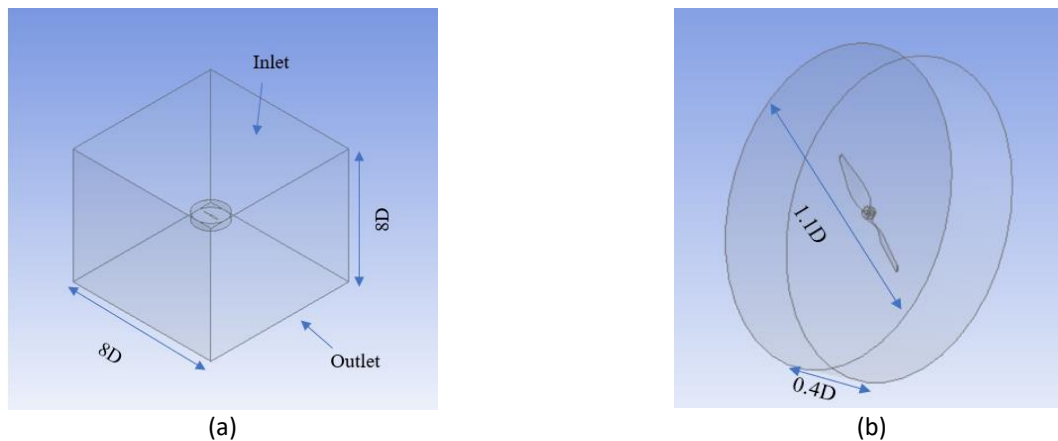
Fig. 3. (a) Stationary domain and boundary condition, (b) Rotating domain and boundary condition

The stationary region's inlet, exit, and outer boundary are far enough away from the propeller to prevent the complete development of the upstream and downstream flow from altering the results of the analysis. Both upstream and downstream of the propeller's origin, the inlet and outlet boundaries are placed 4D (1016 mm). The enclosure for the spinning domain is set at 1.1D (279.4 mm) and 0.4D (101.6 mm). It's critical to choose the flow domain upstream and downstream distances correctly to avoid recirculation of the flow, which can lead to convergence issues.

2.4 Meshing and Modelling

A mesh tool in ANSYS FLUENT was used to create the grid. The grid is significant because it represents the geometry of interest in a unique way. The rate of convergence, the performance derived from the numerical analysis, and the computational time to run the analysis were all directly influenced by the quality of the computational grid. The mesh cell sizes were developed for the current investigation with a narrower range along the blade in the rotating zone and gradually increasing toward the stationary zone. The accuracy of the results is improved by ensuring sufficient grid refinements across the interface. In both stationary and spinning domains, the grid is entirely tetrahedral and unstructured. The decision is based on the rationale that unstructured tetrahedral grids may discretize complex geometries quickly and with minimal user participation. The mesh grid generating information are shown in Table 3. Grid refinement or coarsening - that is, adapting the grid to the physical solution - is easier on an unstructured grid than on a structured grid.

Table 3
Meshing grid for fine mesh

Properties	Details
Element Order	Quadratic
Element Size	80.0 mm
Rotating Domain Size	23 mm
Curvature Normal Angle	40°
Max Size	80.0 mm

Figure 4 depicts the surface mesh of the propeller blade, with figure 4(a) representing the standard mesh, followed by Figure 4(b) for the coarse mesh. Figure 4(c) and 4(d) representing the mid mesh the fine mesh respectively. The numbers of nodes and elements for each mesh are shown in Table 4.
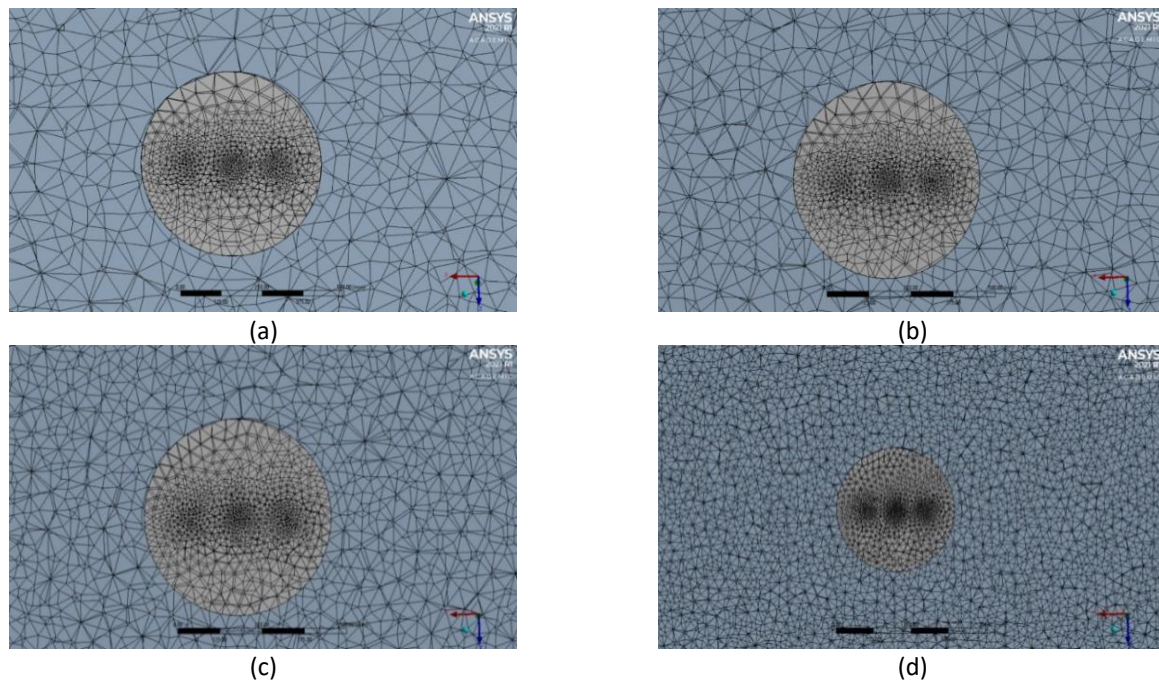
Journal of Advanced Research in Fluid Mechanics and Thermal Sciences
Volume 101, Issue 1 (2023) 160-173

Fig. 4. Meshing of the propeller (a) Standard grid, (b) Coarse grid, (c) Mid-Fine grid, (d) Fine grid

Table 4
Propeller grids

Properties	Details	No. of Elements
Standard Grid	67597	202,755
Coarse Grid	66937	327,713
Mid-Fine Grid	68959	665,827
Fine grid	71012	1,086,451
Standard Grid	67597	202,755

CFD simulations were run with a rotational speed of 4000 RPM to 7000 RPM in the flow conditions listed in Table 5. The free-stream velocity is provided on the inlet border, with a turbulence intensity of 0.1 percent. The wind tunnel intensity measured by [22] and computational domain by [23] is used to determine the turbulence intensity. At the flow exits downstream of the flow domain, outflow boundary conditions were defined. On the walls, a no-slip condition has been established. The MRF is allocated to the domain that includes the rotational speed of the propeller blade. The method is particularly well suited to the analysis, which necessitates the interplay of fixed and revolving frames. Individual zones will have unique rotational or translational speeds allocated to them. A local frame transformation will be applied to the interface between the two zones, allowing the flow variable from one zone to be used by the adjacent zones. The propeller blade and hub walls were likewise designated as rotating, with a velocity of zero in relation to the surrounding cell zone.

A Semi-Implicit Method for Pressure-Linked Equations is used to establish the pressure–velocity coupling (SIMPLE). Momentum and pressure were calculated using the Second Order Upwind method. The gradients were calculated using the First Order Upwind for Turbulent Kinetic Energy and Turbulent Dissipation Rate, as well as the Least Square Cell-based Algorithm. This study's results were accurate thanks to first-order algorithms.

Table 5
Simulation setting

Setting	Nodes
Rotational Speed	4000 RPM to 7000 rpm
Turbulence Intensity	0.1%
Turbulence model	RNG k-ε
Walls	No-slip Condition
Pressure–Velocity Coupling (SIMPLE).	Semi-Implicit Method for Pressure-Linked Equations
Momentum and Pressure Gradient	Second Order Upwind method First Order Upwind for Turbulent Kinetic Energy and Turbulent Dissipation Rate and Least Square Cell-based Algorithm

The RNG k-ε turbulence Model technique uses a global random force to drive small-scale velocity variations and to simulate the effect of large scales on the inertial range eddies. This force is chosen in such a way that the resulting flow field has the same global properties as the flow generated by mean strain. This RNG k-ε model has the same structure as the normal k-ε model, but all the model coefficients are set to different value. The Yakhot version is employed in this work. This turbulence model will be used throughout the research analysis.

3. Results and Discussion
3.1 Trust and Lift Coefficient

The numerical analysis results were compared to available experimental data to validate the simulation test and the quality of the results obtained. For all computational studies, the force and momentum were resolved in a three-coordinate system with parameters *x*, *y*, and *z*. Thrust and torque are defined by the axial force and momentum around the propeller axis. Equations determine the thrust coefficient (K_T) parameter. In the equation, *T* (N) is thrust, *Q* (Nm) is torque, *n* (rps) is the propeller's rotational speed, *D* (m) is the propeller's diameter, and *ρ* (kgm^{-3}) is the density of the fluid.

$$dK_T = \frac{T}{\rho n^2 D^4} \tag{3}$$

Figure 5 shows the plotted data between experimental and simulation data obtained across advance ratio versus thrust coefficient. The trend of thrust coefficient obtained from the experimental data and the normal propeller data are not too different from each other. The normal propeller starts slightly lower than the experimental data with 0.012 difference from each other. Then, the two trends overlap for the second point, and the experimental trend drops slightly while the normal propeller's trend takes longer to fall in trend. From figure 5, the data from the simulation can be deduced that it is correct as the range difference from experimental data and the normal propeller is only from 0.03 to 0.076.

The thrust coefficient of serrated propeller data obtained in the simulation visualized a much lower trend than the experimental and normal propeller across the advance ratio, *J*. The serrated propeller's thrust coefficient has a much lower value than the normal propeller, ranging from 0.06 to 0.081. The highest difference of thrust coefficient between the normal and serrated propeller is at the start of the simulation, which is 0.081. However, the serrated propeller trend in thrust coefficient has much more stability than two other trends, which are linear along with the advance ratio, *J*.
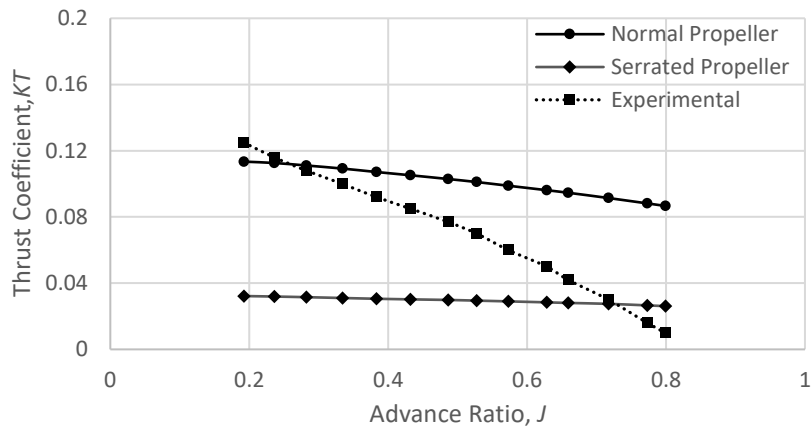
Fig. 5. Thrust coefficient for both propellers and experimental

The normal and serrated propeller produces the lift coefficient in Figure 6 at a constant speed but with a different stage of advance ratio, *J*, bringing out almost the same line of trend as the graph in Figure 5. The normal propeller starts with several times higher value of lift coefficient than the serrated propeller. Then, that's value starts to decrease steadily when the advance ratio increases across the graph. Although the lift coefficient of the serrated propeller has a lower value than the normal propeller, its data almost have the same value when the advance ratio increase gradually. Furthermore, the graph showed that the serrated propeller's lift coefficient's consistency does not increase the advance ratio value.
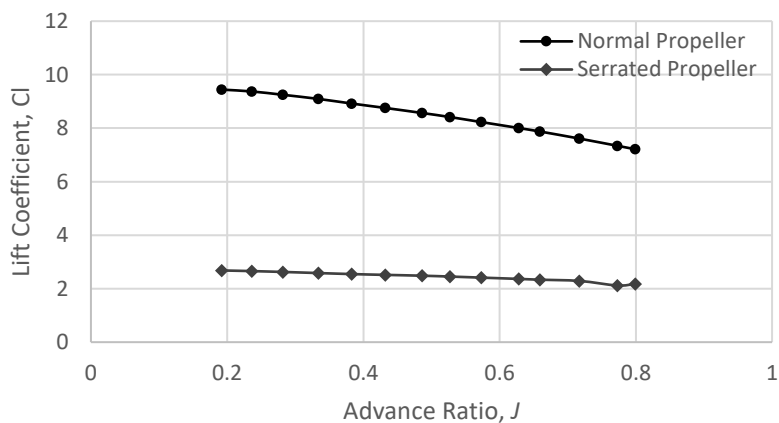

Fig. 6. Lift coefficient between normal and serrated propeller

3.2 Propeller Performance for Different Speeds

Typically, the rotational speeds of the propellers of tiny multirotor drones are normally between 4000 and 7000 rpm, and they are near 5000 rpm in flight. Hence, in this simulation case, the propeller's speed will be taken from 4000 until 7000 rpm to suit the typical case. Then, the normal and serrated propeller's performance will be compared, as shown in Figure 7. The normal propeller showed a significant increase of trend in thrust force value proportional to the growth of speed of the propeller. The thrust force of a normal propeller starts at 2.05 N and gains about 1 N with each ascent in propeller speed except for 4500 rpm with just 0.7 N increment only from the first point.
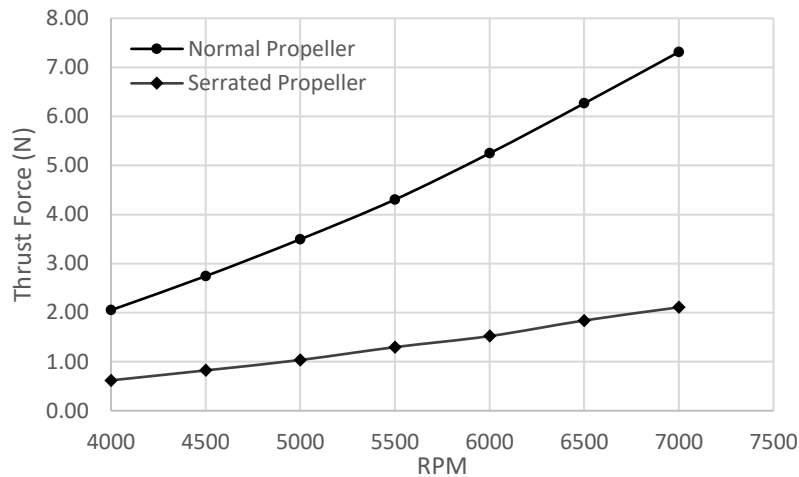
Fig. 6. Thrust force between normal and serrated propellers with different propeller speeds

Nevertheless, the thrust force of the serrated propeller shown in the figure is a much weaker force than the normal propeller. The serrated propeller has only reached 0.62 N for the thrust force at 4000 rpm. The difference of thrust force at 4000 rpm of normal propeller and the serrated propeller is about 1.43 N. Although the trend of thrust force obtained by the serrated propellers shown an increase of force when the speed of propeller increase, the value brought by the serrated propeller far lower than the normal propeller. Based on the figure, the lowest difference value of thrust force between the two propellers will be 4000 rpm. The highest is at 7000 rpm, which is 5.205 N. This shows that even though the speed of the propeller has been increasing from 4000 rpm to 7000 rpm, the thrust performance of the serrated propeller is still lower than the normal propeller. Hence, the serrated feature in the propeller will be constraining the thrust performance, whether at constant speed or with a different speed.

The lift coefficient data for both propellers in Figure 7 show the same trend line compared to Figure 6. However, the value of the lift coefficient of both propellers is much higher than the value obtained in the thrust force region. The lift coefficient of the serrated propeller only produces 1.01 only at the 4000 rpm and extends until 3.44 at the end of the speed of the propeller tested. This value is far lower than the lift coefficient value produced by the normal propeller several times. For comparison, the starting value of the normal propeller in lift coefficient is 3.35, which is a 2.34 difference between them.
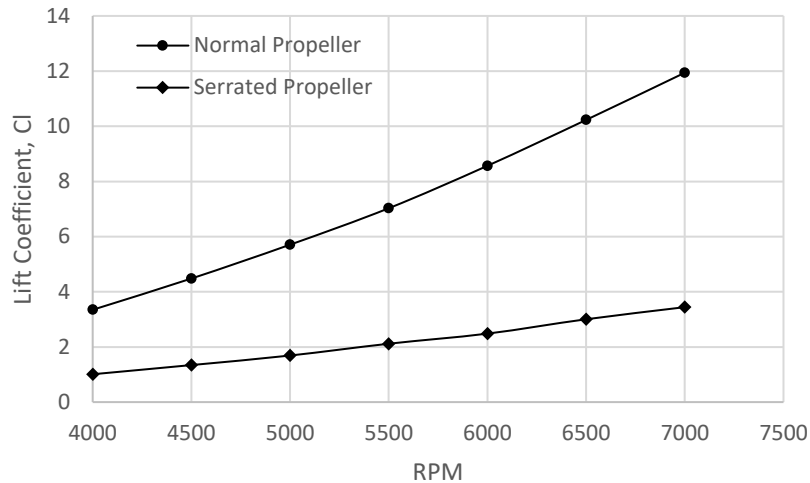
Fig. 7. Lift coefficient between normal and serrated propeller with different propeller speed

3.3 Streamline for Normal and Serrated Propeller

A streamline is a line perpendicular to the direction of instantaneous velocity. In this simulation, the order of the streamline is in the y-direction from the positive value. A streamline is a path that a zero-mass particle travels across the fluid domain. Streamlines begin at each equally spaced node on a particular location. Another way for visualizing the behavior of airflow required for this investigation is to use a streamline. Figure 8-10 shows the streamline with the same propeller speed (6000 rpm) with a different advance ratio, *J* value while Figure 11-13 shows the comparison streamlines for same advance ratio (*J* = 0.486) with different propeller speed.
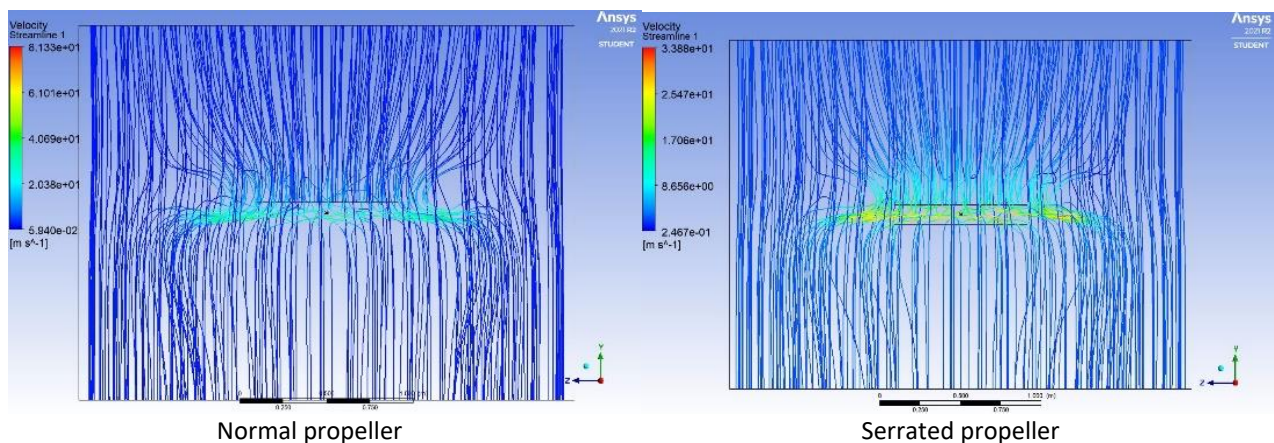

Normal propeller   Serrated propeller
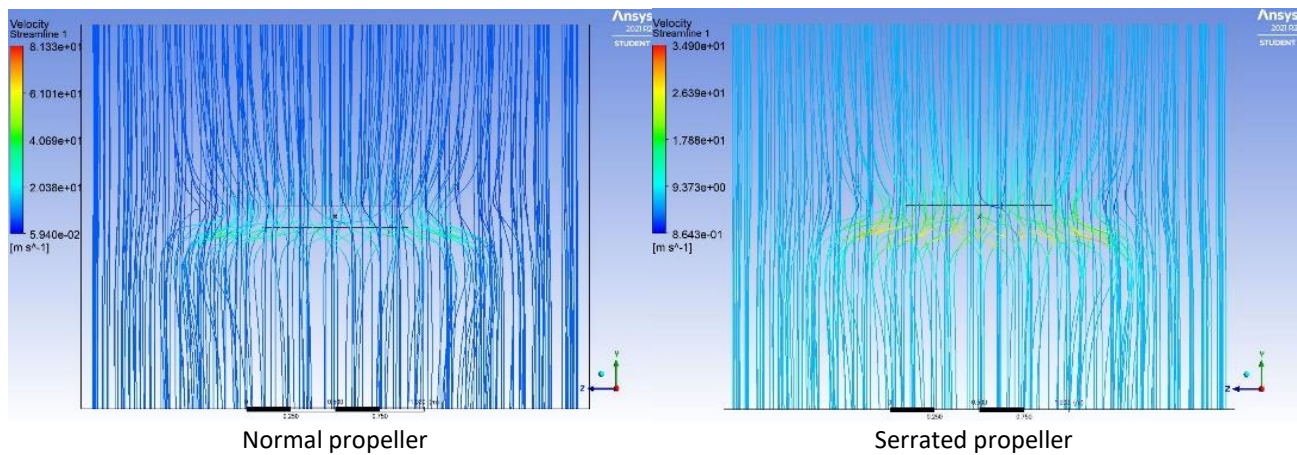**Fig. 8.** Streamline for normal and serrated propeller at J=0.192

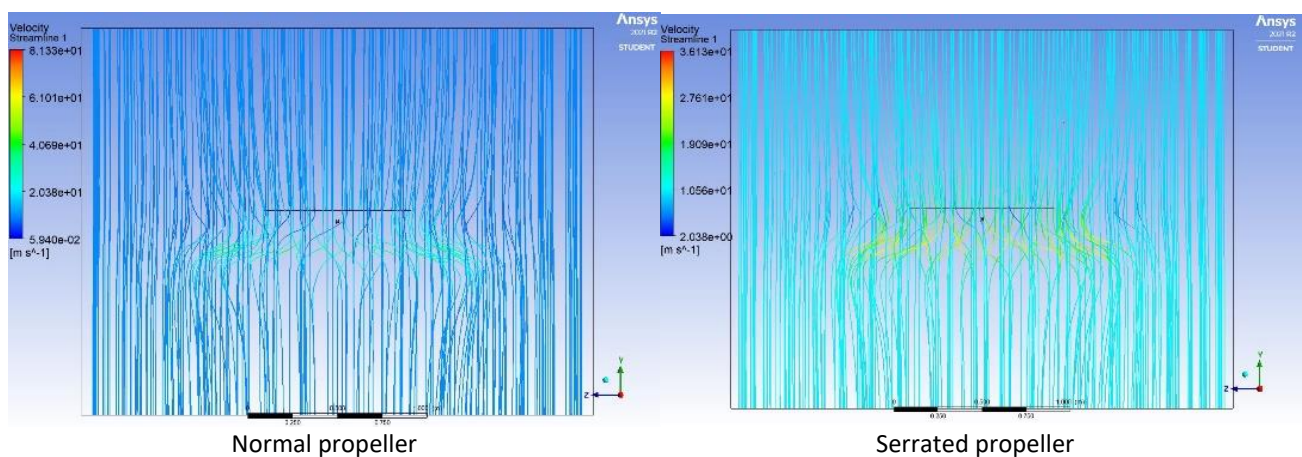**Fig. 9.** Streamline for normal and serrated propeller at J=0.527

Fig. 10. Streamline for normal and serrated propeller at J=0.799

Figure 8 shows the normal propeller has a much higher speed capped than the serrated propeller. Although the serrated propeller shows a much higher colour region than the normal propeller, that region is much lower than the range of velocity streamline in the normal propeller. Comparing with the case for *J* = 0.527 as in Figure 9, the same pattern occurred with the velocity streamline for both propellers. Both propellers have a smooth streamline at the beginning, and it becomes concentrated to the rotating domain and turns into smooth flow again after that. Nonetheless, the normal propeller has a much higher velocity streamline capped than the segregate propeller. This indicates that the normal propeller is much more stable in velocity streamline than the serrated propeller. There is an improvement of the colour region for both propellers for the case of *J* = 0.799 as shown in Figure 10. Both propellers have an increasing velocity streamline in the static domain compared to the propellers for *J* = 0.192 and 0.527. However, the velocity streamlines in the rotating domain remain unchanged throughout *J* values. This indicates that the colour region in the rotating domain for both propellers increases when *J* increases from 0.192 to 0.799. The only change is when the value of *J* increases when the velocity streamlines in the static domain increase in speed.

Fig. 11. Streamline for normal and serrated propeller at 4000 rpm

Fig. 12. Streamline for normal and serrated propeller at 6000 rpm

Fig. 13. Streamline for normal and serrated propeller at 7000 rpm

Another interesting results that will be provide here are the streamlines for different rotation speed. From the results obtained for the simulation of different propellers speed from 4000 to 7000 with a constant advance ratio (J = 0.486), the streamline pattern produced by the normal propeller has more concentration to the rotating domain than the serrated propeller. The serrated propeller makes a bundle of a spot of streamline concentrate to the rotating domain, and between that spot is an empty spot of streamline that is a bit further from each other. Noticeably, both propellers' velocity capped has increased again from the two previous cases. However, the pattern produces by

the propellers remains unchanged when the speed of the propeller is at 6000 rpm. This is because the normal propeller produces a streamline that thickens around the rotating domain because of its high velocity. Nevertheless, the serrated propeller has a minor velocity increase around the rotating domain compared to the normal propeller.

From the result of the various simulation cases between the normal propeller and the serrated propeller, the conclusion that has been derived is that the aerodynamic performance of the normal propeller exceeds the serrated propeller. However, the aerodynamic performance of the serrated propeller is not too low from the normal propeller. Therefore, the serrated propeller performance in various simulations falls below the normal propeller performance. Furthermore, the difference in the aerodynamic performance of serrated propellers becomes noticeably below the normal propeller when the speed of the propeller increases to high velocity. For example, at 7000 rpm, the difference of the thrust force between normal and serrated propellers hit 5.205 N, which is three times the value of serrated thrust force.

4. Conclusion

The computational fluid dynamic approach was employed in this study to quantitatively validate the performance evaluation of the normal and serrated propellers. The simulation analysis was carried out utilizing the transient approach, which estimated the quantity at each time interval. For both propellers, the aerodynamic performance is determined for each time based on a different value of advance ratio *J* but with a constant propeller speed and a constant value of advance ratio J but with a variable propeller speed. For the aims to perform the simulation for the drone propeller with a normal and serrated trailing edge, both propellers were designed and simulated. The first simulation has a constant propeller speed of 6000 rpm and has a different advance ratio *J* from 0.192 to 0.799. The second simulation has different propeller speeds from 4000 rpm to 7000 rpm but has a constant advance ratio *J*, which is 0.486. In determining the propeller's thrust force of the normal and serrated trailing edge, the thrust force of the normal propeller reaches 4.4178 N to the highest 5.7827 N. However, the thrust force of the serrated propeller reaches only 1.4020 N to 1.6422 N only. Subsequently, the value for the thrust force for the normal and serrated propeller in different propeller speeds is from 2.051 N to 7.314 N and from 0.619 N to 2.108 N, respectively. From the simulation and determining the thrust for both types of propellers, it was determined that the thrust force of the normal propeller has more than the serrated trailing edge propeller, notably when both propellers are in high rotating speed between 6000 rpm and 7000 rpm. The normal propeller's thrust force becomes three times that of the serrated propeller when the speed of the propeller reaches 7000 rpm.

References
[1] Brandt, John B., Robert W. Deters, Gavin K. Ananda, Or D. Dantsker, and Michael S. Selig. "UIUC Propeller Database UIUC Propeller Data Site." *University of Illinois at Urbana-Champaign*.
[2] Manshoor, Bukhari, and Amir Khalid. "Numerical investigation of the circle grids fractal flow conditioner for orifice plate flowmeters." In *Applied Mechanics and Materials* 229, (2012): 700-704. https://doi.org/10.4028/www.scientific.net/AMM.229-231.700

[3]   Gill, Rajan, and Raffaello D'andrea. "Propeller thrust and drag in forward flight." In *2017 IEEE Conference on Control Technology and Applications (CCTA)*, (2017): 73-79. https://doi.org/10.1109/CCTA.2017.8062443

[4]   Ning, Zhe, and Hui Hu. "An experimental study on the aerodynamics and aeroacoustic characteristics of small propellers." In *54th AIAA Aerospace Sciences Meeting*, (2016): 1785. https://doi.org/10.2514/6.2016-1785

[5]   Zaman, Izzuddin, Muhammad Mohamed Salleh, and Bukhari Manshoor. "The Application of Multiple Vibration Neutralizers for Vibration Control in Aircraft." *Applied Mechanics and Materials* 629 (2014): 191-196. https://doi.org/10.4028/www.scientific.net/AMM.629.191

[6]   Avallone, F., W. C. P. Van Der Velden, D. Ragni, and D. Casalino. "Noise reduction mechanisms of sawtooth and combed-sawtooth trailing-edge serrations." *Journal of Fluid Mechanics* 848 (2018): 560-591. https://doi.org/10.1017/jfm.2018.377

[7]   Chaitanya, Paruchuri, S. Narayanan, Phillip Joseph, and Jae Wook Kim. "Leading edge serration geometries for significantly enhanced leading edge noise reductions." In *22nd AIAA/CEAS aeroacoustics conference*, (2016): 1-20.

[8]   Pang, Ethan, Aleix Cambray, Djamel Rezgui, Mahdi Azarpeyvand, and Syamir A. Showkat Ali. "Investigation towards a better understanding of noise generation from UAV propellers." In *2018 AIAA/CEAS Aeroacoustics Conference*, (2018): 3450.

[9]   Chin, Wen Jun, Kai Sheng See, Yu Han Ng, Jie Ling Gan, and Sing Yee Lim. "Technologies for Indoor Noise Attenuation: A Short Review." *Progress in Energy and Environment* 9 (2019): 1-10.

[10]   Read, David R., David A. Senzig, Christopher Cutler, Eric Elmore, and Hua He. "Noise Measurement Report: Unconventional Aircraft-Choctaw Nation of Oklahoma: July 2019." *FAA UAS National Airspace Integration Pilot Program*, (2019).

[11]   Gruber, Mathieu, Mahdi Azarpeyvand, and Phillip F. Joseph. "Airfoil trailing edge noise reduction by the introduction of sawtooth and slitted trailing edge geometries." *integration* 10 (2010): 6.

[12]   Lee, Hsiao Mun, Zhenbo Lu, Kian Meng Lim, Jinlong Xie, and Heow Pueh Lee. "Quieter propeller with serrated trailing edge." *Applied Acoustics* 146 (2019): 227-236. https://doi.org/10.1016/j.apacoust.2018.11.020

[13]   Ning, Zhe, Richard W. Wlezien, and Hui Hu. "An experimental study on small UAV propellers with serrated trailing edges." In *47th AIAA fluid dynamics conference*, (2017): 3813. https://doi.org/10.2514/6.2017-3813

[14]   Fischer, Andreas, Franck Bertagnolio, Wen Zhong Shen, and Jesper Madsen. "Noise model for serrated trailing edges compared to wind tunnel measurements." In *Journal of Physics: Conference Series* 753, no. 2, (2016): 022053. https://doi.org/10.1088/1742-6596/753/2/022053

[15]   He, Teo Ting, Muhammed Abdelfattah Sayed Abdelaal, Izzuddin Zaman, Djamal Hissein Didane, and Bukhari Manshoor. "Airflow Analysis of Contra-Rotating Fans Performance by Numerical Simulation." *Technological Advancement in Instrumentation & Human Engineering: Selected papers from ICMER 2021* 882, (2022): 483. https://doi.org/10.1007/978-981-19-1577-2_36

[16]   Gill, Rajan, and Raffaello D'andrea. "Propeller thrust and drag in forward flight." In *2017 IEEE Conference on Control Technology and Applications (CCTA)*, (2017): 73-79. https://doi.org/10.1109/CCTA.2017.8062443

[17]   Bajuri, Muhammad Nur Arham, Djamal Hissein Didane, Mahamat Issa Boukhari, and Bukhari Manshoor. "Computational Fluid Dynamics (CFD) Analysis of Different Sizes of Savonius Rotor Wind Turbine." *Journal of Advanced Research in Applied Mechanics* 94, no. 1 (2022): 7-12. https://doi.org/10.37934/aram.94.1.712

[18]   Gruber, Mathieu, Phillip Joseph, Cyril Polacsek, and Tze Pei Chong. "Noise reduction using combined trailing edge and leading edge serrations in a tandem airfoil experiment." In *18th AIAA/CEAS Aeroacoustics Conference (33rd AIAA Aeroacoustics Conference)*,(2012): 2134.

[19]   Niknahad, Ali. "Numerical study and comparison of turbulent parameters of simple, triangular, and circular vortex generators equipped airfoil model." *Journal of Advanced Research in Numerical Heat Transfer* 8, no. 1 (2022): 1-18.

[20]   Halmy, Muhammad Syahmy Mohd, Djamal Hissein Didane, Lukmon Owolabi Afolabi, and Sami Al-Alimi. "Computational Fluid Dynamics (CFD) Study on the Effect of the Number of Blades on the Performance of Double-Stage Savonius Rotor." *Cfd Letters* 13, no. 4 (2021): 1-10. https://doi.org/10.37934/cfdl.13.4.110

[21]   Kutty, Hairuniza Ahmed, and Parvathy Rajendran. "3D CFD simulation and experimental validation of small APC slow flyer propeller blade." *Aerospace* 4, no. 1 (2017): 10. https://doi.org/10.3390/aerospace4010010

[22]   Chen, Qingyan. "Comparison of different k-ε models for indoor air flow computations." *Numerical Heat Transfer, Part B Fundamentals* 28, no. 3 (1995): 353-369.

[23]   Meile, Walter, Günter Brenn, Aaron Reppenhagen, Bernhard Lechner, and Anton Fuchs. "Experiments and numerical simulations on the aerodynamics of the Ahmed body." *CFD letters* 3, no. 1 (2011): 32-39.